Modeling Snow Ablation over the Western United States Mountains: Patterns and Controlling Factors

Mu Xiao[1], Sarith P. Mahanama[2,3], Yongkang Xue[1], Fei Chen[4] and Dennis P. Lettenmaier[1]

[1]Department of Geography, University of California, Los Angeles, CA

[2]Global Modeling and Assimilation Office, NASA GSFC, Greenbelt, MD

[3]Science Systems and Applications, InC., Lanham, MD

[4]Research Application Laboratory, National Center for Atmospheric Research, Boulder, CO

Corresponding author: Dennis P. Lettenmaier, dlettenm@ucla.edu

Abstract

Compared to differences in snow accumulation predicted by widely-used hydrological models, there is a much greater divergence among otherwise "good" models in their simulation of snow ablation process. Here, we explore differences in the performance of VIC, Noah-MP, Catchment and SSiB3 in their ability to reproduce observed snow water equivalent (SWE) during the ablation season at ten SNOTEL stations over 1992-2012. During the ablation period net radiation generally has stronger correlations with observed melt rates than does air temperature. Average ablation rates tend to be higher (in both model predictions and observations) at stations with large accumulated SWE. The differences in the dates of last snow between models and observations range from several days to approximately a month (on average 5.1 days earlier than in observations). If the surface cover in the models is changed from observed vegetation to bare

soil in all the models, only the melt rate of the VIC model increases. The differences in responses of models to canopy removal are directly related to snowpack energy inputs, which are further affected by different algorithms for surface albedo and energy allocation across the models. Finally, we find that the melt rates become higher in VIC and lower in Noah-MP if the shrub/grass present at the observation sites is switched to trees.

1.0 Introduction

Snow is a dominant aspect of the land surface hydrological cycle of the Western U.S., especially in the headwaters of the major river basins. Snowpacks store precipitation during the cold season and release water via melt during the following warm season, effectively providing a natural reservoir that shifts the timing of peak runoff relative to precipitation by several months. In most Western U.S. river basins, snow is the largest (seasonally varying) water storage component (Mote et al. 2005). Li et al. (2017) found that 53% of the runoff over the Western U.S. originates from melting snowpacks, a number that increases to 70% in the mountainous parts of the region. In relatively dry and heavily-populated Southern California, more than half the water supply is derived from snowmelt from remote mountainous sources (Waliser et al. 2011). As temperatures have warmed in recent decades, snowpack behavior and corresponding hydrological processes have been severely affected. For instance, Mote et al. (2018) report that over 90% of the snow monitoring stations across the Western U.S. with long-term records have shown declines over 1955-2014. As temperatures continue to warm, Rauscher et al. (2008) estimate that snowmelt-driven runoff over the West could occur as much as two months earlier than it has historically.

Despite its importance to surface water hydrology, determining representations of the complicated mechanisms that govern snowpack accumulation and ablation in hydrologic models remain challenging. Given both the scientific challenges and practical implications, Dozier et al. (2016) have argued that estimation of the spatial distribution of SWE over mountainous areas is the most important unsolved issue in snow hydrology. The problem is complicated by the fact that snow depth variability can be caused by a mix of multiple process at various spatial scales

(Clark et al. 2011). On the other hand, snow accumulation over the Western U.S. can usually be predicted by the accumulated precipitation occurring during the winter at temperatures below a threshold (typically slightly greater than 0˚C on daily average). For instance, Figure 1(a) shows that SWE estimated using a very simple rule that approximates the seasonal maximum SWE as the accumulation of all precipitation that occurs during the winter season below a fixed (daily average) temperature yields plausible predications of maximum winter snow accumulations at a great number of SNOTEL sites. Figure 1(c) shows, when the models are initialized with the observed seasonal SWE maxima, the variations in ablation rates are substantial, and can lead to variations in the predicted date of last SWE that exceed one month.

Here, we explore, in off-line simulations, the ablation season performance of four energy-based snow models that are widely used in macroscale hydrologic models and coupled land-atmosphere models. In particular, we examine their ability to reproduce observed snow ablation rates at selected Snow Telemetry (SNOTEL) sites (snow pillows operated by Natural Resources Conservation Service (NRCS)) across the Western U.S. We examine differences among the snow models (and between models and observations) during the ablation period by analyzing the factors that control snow ablation. The remainder of the paper is organized as follows: section 2 describes the data and models used in the comparisons. We report results in section 3, with discussion and interpretation in section 4. Finally, our conclusions are presented in section 5.

2.0 Data and Methods

2.1 Snow observations and ablation estimate

The USDA Natural Resources Conservation Service (NRCS) Snow Survey and Water Supply Forecasting Program (https://www.wcc.nrcs.usda.gov/) has a network of 808 automated SNOTEL

stations in the Western States. Starting in the early 1980s, the SNOTEL stations began to report daily snow water equivalent (SWE) using snow pillows (which weigh the accumulated snowpack continuously in time), as well as (most sites) daily precipitation, and daily maximum and minimum temperature. We selected 10 SNOTEL stations distributed over the Western United States (Figure 2) whose data are of high quality (missing values less than 5%). The snow types in the western mountainous regions are either Alpine or Maritime according to (Sturm et al. 1995) and the sites we selected include both types (three are Alpine and seven are Maritime). These stations form the basis for our analyses and station names and elevations are given in Table 1.

In order to evaluate snow ablation characteristics, we first need to define the ablation process and melt rates. Previous studies have attempted to employ snow depth and SWE values to determine the ablation period (Dyer and Mote 2007; Trujillo and Molotch 2014). Our main objectives are to explore the behavior and the controlling factors during the snow melt season and to determine the bias and uncertainty among the models in estimating SWE during this period. Therefore, we use the SWE-based definition of Trujillo and Molotch (2014), which is: for each water year (Oct-Sep), the ablation period is the time from the date of maximum SWE to the last day of snow existence (SWE>0). Further, we extract the 20^{th}-80^{th}-quantile of the ablation period, which we define as the period from the date when 80% of the maximum accumulated SWE remains to the date when 20% of SWE remains. Based on our exploratory analysis, focusing on this central portion of the melt period seems to provide a representation of the ablation process that minimizes unusual conditions near the beginning and end of the melt period (e.g., occasional accumulation events early in the melt period, and very warm conditions with partial snow cover late in the melt period). Therefore, In the analyses we report below, our results are

based on the 20^{th}-80^{th}-quantile definition unless stated otherwise. Accordingly, we calculate snow ablation rates for each year the 80^{th}-quantile of SWE minus the 20^{th}-quantile of SWE divided by the number of days between the corresponding dates.

2.2 Land surface models

We examined simulations of SWE using four Land Surface Models (LSMs) : Variable Infiltration Capacity (VIC), Noah Multi-Parameterization (Noah-MP), Catchment, and Simplified SiB version 3 (SSiB3), all of which have been applied previously in numerous snow-related studies (e.g. Tan et al. 2011; Shi et al. 2013; Chen et al. 2014; Newman et al. 2014; Xia et al. 2016; Magand et al. 2013; Xue et al. 2018; Oaida et al. 2015; Cortés et al. 2016; Rutter et al. 2009 among many others). The relevant archival references for the snow algorithms in the four models are: VIC (Andreadis et al. 2009); Noah-MP (Niu et al. 2011); Catchment (Stieglitz et al. 2001); and SSiB3 (Sun et al. 1999; Xue et al. 2003). The key features of the snow algorithms in each of the model are summarized in Table 2. We also provide brief descriptions of each model below.

VIC is a physical-based, macroscale hydrologic model with an energy-based snow module that explicitly accounts for snow accumulation and ablation in the vegetation canopy (Andreadis et al. 2009). It represents two layers in the vertical (one for thin snowpacks) – a relatively thin surface layer, and a deeper pack layer. The VIC model represents the snow interception effect of the canopy and fractional snow cover is represented as well. Further, shortwave attenuation through the canopy is also represented using a Beers Law formulation (Andreasis et al., 2009). Snow albedo (α) in VIC decays with time from snowfall (t) according to a scaled exponential relationship based on USACE (1956).

115 Noah-MP has much different physics than the original Noah LSM (Chen and Dudhia 2001;
116 Ek et al. 2003) to the extent that it essentially is a different model. Regarding the snowpack
117 modeling, the Noah-MP snow model partitions the snowpack into up to three layers according
118 to the snow depth and snow cover fraction as determined by snow density, snow depth and
119 ground roughness length. Noah-MP relates the vegetation cover fraction to prescribed LAI values
120 (Niu et al. 2011). To calculate the energy terms at the snow surface, Noah-MP utilizes a "semi-
121 tile" scheme to calculate the energy balance and solves for the snow temperature over vegetated
122 and bare fractions separately. Shortwave radiation fluxes (ground- and canopy- absorbed) are
123 computed over the entire grid cell assuming the canopy is evenly distributed; the other fluxes
124 (ground heat, latent heat, sensible heat, and longwave radiation) are calculated for bare soil and
125 vegetated parts of a "tile" (grid cell) separately. The scheme in Noah-MP, which considers gap
126 probabilities for shortwave radiation transfer, is designed to avoid over-shading effect of the
127 canopy. The snow albedo is adopted from the CLASS model (Verseghy 1991), which accounts for
128 snow age, grain size, and accumulated debris on the snow surface.
129 Catchment incorporates a three-layer snow module to account for snowpack growth and
130 ablation (Stieglitz et al. 2001). Catchment determines the net solar radiation flux using estimates
131 of surface albedo; this albedo is calculated separately for the snow-covered and snow-free
132 fractions of the land element, and vegetation "sticking out" of the snowpack modifies the albedo
133 in the snow-covered fraction. Catchment does not separate downward solar radiation according
134 to vegetated and bare-soil surfaces, i.e. it does not use a two-stream scheme as do the other
135 three models. Rather, it first calculates the average surface albedo (with and without snow) and
136 computes the net solar radiation for the entire surface. In Catchment, snowpack albedo is

parameterized as a function of snow surface aging (Stieglitz et al. 2001). Catchment's snow free parameterization is designed to match MODIS climatological mean albedo at the location at any given time. The snow parameterization in Catchment (Stieglitz et al. 2001) uses a 13 mm threshold of SWE to compute the snow-covered fraction, i.e. if SWE is greater than or equal to 13 mm, the entire tile is assumed to be snow covered.

SSiB3 uses the snow-atmosphere-soil transfer (SAST) model of Sun et al. (1999). SAST uses up-to three layers to represent snow in vegetation-free areas and under canopies. Snow albedo decays with snow age as adjusted by cloud cover and sun elevation angle. The land surface in SSiB3 is divided into canopy and bare soil parts according to the vegetation fraction in the same way as is done by SSiB for snow-free areas. The snow energy fluxes and surface soil temperature are solved simultaneously to guarantee energy conservation at each time step. SSiB3 employs (fixed) monthly-varying parameters for vegetation cover fraction and leaf area index, both of which are also dependent on the pre-defined vegetation type (Sellers et al. 1996).

2.3 Forcings and experimental set-up

We extracted daily meteorological observations (daily precipitation and temperature maxima and minima) at 10 selected SNOTEL sites. Because trends in daily temperature minimum (Tmin) at SNOTEL sites over the west have been reported to be artificially amplified (Oyler et al. 2015), we performed another experiments to examine the possible effects of these artificial changes. We corrected the Tmin from the SNOTEL records using another temporally consistent data, the Hamlet and Lettenmaier (H&L) data (Hamlet and Lettenmaier 2005), which we extended to 2014 (Mote et al. 2018). We adjusted Tmin records extracted from SNOTEL after the year 1997, when the artificial modification first occurred (Oyler et al. 2015), to guarantee that

159 the average differences in monthly Tmin between SNOTEL and H&L were the same for before
160 and after 1997. We then tested the models with the adjusted forcings. We found that the results
161 show no obvious differences relative to our base experiments (Figures S1-S2). Therefore, we used
162 the original temperature records from each of the SNOTEL sites in our analysis. We used wind
163 speed from the Livneh data set (Livneh et al. 2013) which is interpolated from the lowest layer of
164 the NCEP/NCAR reanalysis (Kalnay et al. 1996). We applied the Mountain Climate (MTCLIM)
165 algorithms (Hungerford et al. 1989) as incorporated in the VIC model (Bohn et al. 2013) at each
166 station to produce hourly precipitation and temperature, downward solar and longwave
167 radiation, pressure and humidity forcings. Our study period is from 1992 to 2012, which was
168 determined by the availability of the SNOTEL meteorological observations and the temporal
169 coverage of the Livneh dataset.

170 To evaluate the magnitude and nature of differences in ablation rates among the models,
171 we manually adjusted the SWE predictions for all models to match the SNOTEL annual maxima
172 for each water year (i.e. within every year, when the SNOTEL observation reached its annual
173 maximum, we replaced the simulated SWE on that day with the observed value). We also
174 performed sensitivity tests to examine the possibility of carryover effects associated with
175 snowpack cold content and liquid water storage, and we found the differences to be negligible
176 (Figure S3). For each model, we performed model simulations from each year's observed date of
177 maximum SWE through the (model's) date of last SWE, and we repeated the process for the next
178 water year. This procedure allowed us to reduce the differences among models in the
179 accumulation period.

We determined the vegetation type at each site using site images provided by NRCS (Figure S4). As shown in the photos, the snow pillows are all in openings. We classified Css Lab (Site 8) as grass, and all other sites as shrub. Two of the 10 sites (Hand Creek and Pike Creek) did not have site images and we choose shrub as their vegetation cover according to Google Earth satellite imagery. We specifically extracted the heat fluxes (net-radiation, sensible heat, latent heat, etc.) at the snow surface (below the canopy) as well as above the canopy from each model to evaluate their effects on ablation process.

For shrub and grass vegetation types, the differences between energy fluxes above and below canopy generally are small (in part because snow covers the vegetation through much of the ablation period in the models). Therefore, we performed an experiment where the vegetation cover at all sites was set to trees, and compared the energy terms above and below canopy with the runs corresponding to the vegetation actually present at each site (see discussion section).

3.0 Results

3.1 Ablation rates

Figure 3 shows the average ablation rates (calculated as described in section 2.1) at each of the SNOTEL sites for over the entire study period. Overall, the Catchment model produced the best estimates as compared with observations in terms of Mean Absolute Error (MAE). VIC, Noah-MP and SSiB generally have melt rates that were biased high with one exception (site 10 for SSiB). The overall bias across all models is slightly positive (the observations have lower ablation rates than the simulations) while only Catchment has generally negative biases. The multi-model ensemble-average yielded melt rates with MAEs that were higher than those of the best model

(Catchment). The station-averaged errors (model minus observed averaged over years) in the estimated last day of the ablation period were -3.6 (VIC), -6.1 (Noah-MP), -5.0 (SSiB), 0.3 (Catchment) and -5.1 (model-average) days, respectively. However, the station averages obscure substantial variability, as VIC differences ranged from -10.9 to 2.6 days across the 10 stations, Noah-MP from -12.6 to -0.1, SSiB from -12.7 to 3.2, Catchment from -3.7 to 4.3 and model-avg from -10.9 to -0.8 days.

Table 3 summarizes the climatologies of the 10 SNOTEL sites in terms of average temperature and maximum annual SWE. Considering the ablation rates in Figure 3 and the maximum SWE values in the table, the stations that have the highest SWE accumulations also tend to experience faster melt rates. Figure 4 reports the correlation coefficients between average annual maximum SWE and average ablation rates for the observations and modeled results across all 10 stations. Linear regression relationships are also plotted in the figure. The results from observations are highly correlated (r=0.97) as are the Catchment results. The R-values of other models range from 0.85 to 0.97. One possible reason to explain the correlations is that the low SWE stations melt their snow before the period of highest available energy (late spring and early summer). As the downward solar radiation increases seasonally, only those stations with higher SWE remain snow covered. The snowpack at these high SWE stations receives more downward shortwave radiation later in the year, and thus tends to have higher ablation rates. We do note however that the cloud cover might cause exceptions to this general trend.

3.2 Dependence on temperature and net-radiation

Figure 5 shows the results of linear regressions of the computed ablation rates on the average temperature during the melt season along with the correlation coefficients for observed and simulated results. Overall, the correlations between ablation and temperature are high, with values from observations ranging from 0.51 to 0.92 with an average of 0.73. The model results also show more or less linear dependences, with only 6% of the r-values across all stations and models less than 0.6. Although there are some deviations for individual models, the model-averaged results in general capture the observed relationships between temperature and ablation rates at each of the SNOTEL sites.

Figure 6 is similar to Figure 5, except with temperature replaced with net radiation at the snow surface. There is no observation-based net-radiation, instead we used the average net radiation from the four LSMs as a surrogate for observations. The correlation coefficients in Figure 6 generally are higher than in Figure 5. In particular, the station average for both observation-based (0.93 in the last subplot of Fig 6) and model-averaged (0.97 in the last subplot of Fig 6) both are substantially higher than those in Figure 5 (0.73 for observed analysis and 0.69 for model average). Statistically, 61% of the r-values in Figure 5 are greater than 0.8, and this percentage increases to 94% in the Figure 6 net-radiation correlation results. This result should not be surprising as net radiation is the dominant source of melt energy, and temperature appears only in the net longwave radiation component of net radiation (which generally is much smaller than net shortwave during the melt season).

We also performed a similar test of the relationship between wind speed and ablation rate. We found that correlations were weak in most cases. Only three SNOTEL sites have statistically significant ($p<0.05$) correlations between wind speed and ablation rate (Figure S5).

At those three sites, there is a (weak) inverse relationship between net-radiation and wind speed, which likely leads to the apparent relationship with wind speed. We do note that the source of our wind speed data is the surface level wind in the NCEP-NCAR reanalysis (Kalnay et al. 1996) which is a coarse scale product (2.5 degrees latitude by longitude) which is unable to capture local scale variations in wind speed. However, a larger factor likely is that wind speed is a determinant of turbulent fluxes (latent and sensible heat) which generally are of opposite sign during the ablation period, and therefore tend to be small in magnitude relative to net radiation. During rain-on-snow events (which do occur occasionally during the ablation period) latent heat flux can be an important contributor to melt (Moore and Owens 1984; Guan et al. 2016). However, such events occur infrequently enough, and are of small enough magnitude during the melt period, that they appear not to have a major effect on ablation.

3.3 Energy components

To better understand the factors that control snowmelt, we need to identify the sources of melt energy. The surface energy budget equation (which is represented directly in all four of the LSMs), can be expressed as:

$$Q_M = Rn + SH + LH + GH + Q_A,$$

where Q_M is the energy absorbed by the snowpack (melt energy), Rn is the net radiation, SH is the sensible heat flux, LH is the latent heat flux, GH is the ground heat flux, and Q_A is the energy advected to the snowpack by precipitation (the directions of these energy terms in the equation are all downward). GH and Q_A are usually small during the melt season and we neglect them. We focus here on Rn, SH, LH, and their sum Q_M (Rn + SH + LH) which accounts for most of the melt

energy. All of the energy terms in this section are the fluxes at the snow surface unless stated otherwise.

We show simulated net radiation, sensible heat and latent heat fluxes for each model and station in Figure 7. Net shortwave, net longwave and net downward radiation are shown in Figure 8. In Figure 7, the white circles indicate Q_M, the melt energy. The four models all have positive sensible heat fluxes, which means that energy is transferred from the air to the surface. Of the four models, Noah-MP produces the most net radiation. However, its ablation rate is not the highest, as it also has large negative latent heat fluxes. Generally, VIC and SSiB have the largest melt energy Q_M at those selected sites, but only VIC produces higher ablation rates. SSiB allocates more energy in the snowpack to ground heat flux, which reduces the energy available for ablation. The estimated net longwave radiation among all models is generally similar. Therefore, the net-radiation differences are largely attributable to net shortwave radiation differences, which in turn are primarily attributable to differences in ground surface albedo and vegetation shading effect among the models. We discuss this further in the following section.

4.0 Discussion

4.1 Vegetation cover effects

During the ablation process, the vegetation canopy, if present, can play an important role in energy transfer to the snowpack. Usually (although not always) SNOTEL sites are located in clearings surrounded with short vegetation that is covered by snow for most of the ablation season. Each model's vegetation cover mechanism is distinct as is its representation of the interaction between canopy and land surface and snow on and under vegetation (described in section 2.2). Furthermore, the models have different representations of how much snow can be

intercepted by the vegetation canopy and the energetics of snow on and below the canopy. Their representations of the effects of the canopy on absorption and re-radiation of solar radiation, as well as the effects of the canopy on wind, and hence under-canopy turbulent fluxes also vary. Arguably the first consideration (snow interception) is less important during the ablation season than is the second (vegetation effects on under-canopy net radiation and turbulent fluxes).

In order to evaluate the canopy effects and corresponding model behaviors, we performed a parallel set of simulations, whose setup was the same as the baseline described above but with the canopy cover removed. Figure 9 shows the ablation rates that resulted from the no vegetation experiment (note that the melt rates calculated from the observations are identical to the results shown in Figure 3 as they require no assumptions about vegetation). From Figure 9, we see that without the canopy cover, the ablation rate in VIC increases. Melt rates for Noah-MP, Catchment and SSiB are reduced relative to their baseline runs when the vegetation is removed. Removal of vegetation results in degradation of VIC performance relative to observations (MAE increases to 10.29 mm/day from 8.25 mm/day in the baseline experiment). Noah-MP and SSiB have smaller MAEs in the no canopy condition relative to the baseline. The MAE of Catchment increases slightly in the no vegetation simulation. We do note that at some of the sites (Olallie Meadows, Banner Summer, Blue Mountain Spring, and Silver Creek in particular; Figure S4) a review of photos of the SNOTEL sites shows the presence of some vegetation in the vicinity of the snow pillow, i.e., the no vegetation assumption may not be entirely appropriate. In those cases, the no vegetation assumption is best interpreted as an end point for comparison with the vegetated base runs.

309 To explain the cause and effect of different model behaviors, we need to analyze the
310 energy components in the no vegetation simulations and relate them to the models' own
311 algorithms. Figure 10 shows the energy terms at snow surface and Figure 11 presents the
312 breakdown of net radiation (net shortwave and net longwave) for all models from the no
313 vegetation simulations. The behavior of models' ablation rates matches the responses of Q_M with
314 no canopy in Figure 10: VIC shows increased Q_M whereas in the other three models Q_M decreases.
315 The last panel (stn-avg) of Figure 10 shows the overall average responses of Rn, LH and SH. Rn
316 during the ablation period decreases slightly in VIC and Noah-MP without canopy while it
317 increases in SSiB3 and Catchment (Figure 11). LH does not reflect obvious effects of removing the
318 canopy cover. SH decreases in SSiB3 and Catchment while it increases in VIC. SH in Noah-MP is
319 similar in the no-veg and baseline simulations.
320 Because Rn is the dominant factor that controls the ablation process, we further
321 investigated the Rn responses of the models when the canopy cover was removed. As noted
322 above, Rn decreases in VIC and Noah-MP but increases in SSiB3 and Catchment. Rn differences
323 are mostly associated with net shortwave (net-SW) differences as the changes in net longwave
324 are small (Figure 11). Net-SW is strongly influenced by ground albedo, which is essentially the
325 snow surface albedo during the 20-80-quantile ablation period. Snow albedo and incoming
326 shortwave fluxes are not much affected without shrub/grass in VIC and Catchment. Therefore,
327 the surface net SW of these two models are almost identical in that case. However, removing the
328 canopy changes roughness height in those two models thereby affecting the allocation of energy
329 to SH, and that causes changes in the ablation periods (earlier melting for VIC and later for
330 Catchment). The snowpack can absorb more energy when the snow season is longer as incoming

solar radiation increases through the ablation season. Therefore, Rn in VIC and Catchment show similar responses under no-veg scenarios. In Noah-MP, the shrub/grass would absorb extra shortwave energy as incoming solar to heat the snow surface (Niu and Yang 2007). Because the shading effect in Noah-MP is designed to avoid overestimation (Niu et al. 2011), the solar radiation absorbed by the ground in Noah-MP does not increase substantially when the canopy is removed. One effect of the Noah-MP parameterization is that removing the vegetation cover results in a decrease in shortwave flux absorbed by the snow surface, which leads to less net SW in Noah-MP. SSiB has the greatest increase in net-SW when the canopy is removed, which is traceable to its relatively large shading effect even for short vegetation (shrubs and grass). For VIC, Noah-MP and Catchment, the shading effect associated with shrub and grassland are less obvious. The controlling factor in the differences in Rn of these three models is therefore the ground surface albedo algorithm in short vegetation scenario. We conducted another experiment to further explore vegetation shading effects as reported in the following subsection.

4.2 Energy above and below trees

We performed another vegetation scenario to further elucidate the differences between energy fluxes above and below the canopy during the ablation season. As noted above, the vegetation at SNOTEL sites (as contrasted in most cases with the surrounding area) is either grass or shrubs, both of which have only modest effects on snow ablation. A much larger contrast would be expected between forested and no vegetation conditions. Therefore, we created a scenario where we prescribe needleleaf trees as the canopy type for all SNOTEL sites to guarantee that a shading effect occurs during the ablation season (VIC, for instance, does not employ a shading mechanism for shrubs and grass). However, the offline version of Catchment

353 does not include wind attenuation for trees and performs better when forced with modified
354 (attenuated) near-surface wind speed. Because we are using wind speed from the NCEP/NCAR
355 reanalysis product, the wind forcing arguably is a plausible approximation of near-surface wind
356 for short canopies (grass and shrub) scenarios but not for under forest. In exploratory simulations
357 we found this leads to unrealistically high melt rates in Catchment. For this reason, in the
358 simulations we report below, we only tested VIC, Noah-MP and SSiB3. The related
359 parameterization of needleleaf trees (height, LAI) are retained as the default in each model.

360 Figure 12 shows the average ablation rates across all stations and the Rn, LH and SH from
361 VIC, Noah-MP and SSiB3 extracted from the tree simulation. For all the three models, the
362 magnitudes of changes in melt rate between canopy-covered and no-veg will increase if we
363 switch shrub/grass to trees in the simulation. Compared to ablation rates from bare-soil
364 experiments (VIC 26.3, Noah-MP 24.0, SSiB 18.5 as in Figure 9), switching shrub/grass to trees
365 leads to slower ablation in VIC (tree: 21.4; shrub/grass: 24.3) and faster in Noah-MP (tree: 26.4;
366 shrub/grass: 25.0). The changes in SSiB snow ablation are modest (tree: 22.8; shrub/grass: 22.9).
367 The middle panel shows the energy terms at the snow surface below the canopy and the right
368 panel shows the fluxes at the top of the canopy. The Rn below the canopy in all three models are
369 smaller compared to the Rn of the entire canopy-cover surface at the top of the trees, which
370 results from the attenuation of shortwave transmission through the forest for the models. Also,
371 the canopy in Noah-MP can absorb additional shortwave (SW) energy for the surface (i.e. total
372 absorbed SW radiation equals the sum of SW absorbed by canopy and SW absorbed by the
373 ground), which results in higher Rn for the entire canopy-covered surface than Rn at the ground.
374 The sensible heat varies differently among the models. VIC produces upward sensible heat flux

at the top of the canopy, which implies that the surface is warming the atmosphere. Having upward sensible heat flux over the forest is not unrealistic, as shown by ground observations reported in Fig.9 in Chen et al. (2014). In SSiB3, the sensible heat exceeds net radiation, which implies that the air below the trees transfers considerable heat to the snow. The forest effect on ablation below the trees can shift depending on the relative importance of the shading and wind attenuation effects (Lundquist et al. 2013). The differences among the models (which are caused by the combination of different solar radiation attenuation effects, absorbed net shortwave associated with different surface albedos, and various algorithms of energy allocated to SH) point to the need for high-quality, broad-coverage radiative and flux data above and below forest canopies.

4.3 Interpretation

Some patterns of the ablation process as revealed by our multi-model expriements are in good agreement with previous studies. In Figure 4 we show that sites with higher SWE accumulation generally have higher ablation rates, because those stations experience higher daily incoming solar radiation at the time of peak SWE, which generally is later in the year than for stations with lower peak SWE. Musselman et al. (2017) argue that in a warmer climate, snow ablation rates in the western U.S. will decrease for this reason (peak SWE will occur at a time of generally lower incoming solar radiation), which is consistent with our results. We also demonstrate that the net-radiation at the snow surface has a stronger effect on ablation than temperature (Figure 5 & 6). This result is consistent with Painter et al. (2018) who show (in the context of the role of dust on snowmelt rates) that radiative forcings are a much more important determinant of snowmelt rates that control the rising limb of the hydrograph in Upper Colorado's

spring runoff than is temperature. One could in fact argue that the only reason that the temperature correlations in Figure 5 are as high as they are is that high temperatures tend to be correlated with clear sky conditions during the melt period, which in turn are associated with high downward solar radiation.

By comparing the performance of the land surface models in all the scenarios, considerable differences and variations are apparent in the models' responses. Given that estimating the spatial distribution of SWE in mountain areas remains an important unsolved question in snow hydrology (Dozier et al. 2016), it is not surprising that there are large uncertainties amongst different models. Our results show, not surprisingly, that the presence or absence of forest leads to relatively large differences among models because of differences among models in the way they treat the effects of forest cover on surface energy components. Differences in short canopy cover (shrub/grassland) lead to more modest differences among the models in their simulation of surface processes. Land surface models utilize simplified equations to represent complicated snow process, and the simplifications vary among models. For example, longwave radiation and reflection can play important roles in canopy-dense areas. However, this is usually not well represented in macro-scale land surface models. In this respect, the paucity of high-quality energy flux observations (below/above the canopy, among different types of land cover) is a strong constraint on model improvements. The differences among models we report here argue for better use of existing field data by incorporating observations that have been collected by different parties. Such use of "crowd sourced" field observations to evaluate model predictions arguable would be more cost-effective than comprehensive field campaigns.

5 Summary and Conclusions

We employed four widely used energy-based LSM snow models in offline simulations to explore differences in melt season ablation rates at 10 SNOTEL stations across the Western United States. We extracted precipitation and temperature data from in-situ observations at each of the SNOTEL sites. We manually adjusted the maximum annual SWE value each year to match the in-situ observations for the purpose of focusing on differences in model performance during the ablation periods. We assessed the linear dependence of the ablation rate on two major atmospheric factors: temperature and radiation. We also performed a no vegetation scenario and an artificial forest scenario to study the effects of vegetation on ablation rates at each of the SNOTEL sites. Based on these experiments, we conclude that:

1) On average, the four LSMs produce ablation rates that match observations at the SNOTEL sites in the baseline experiments plausibly well. The average MAE for all models is 5.4 mm/day (28% of the observed average ablation rate across the 10 stations), ranging from 3.6 mm/day (Catchment) to 8.3 mm/day (VIC). Catchment is the only model that has negative bias (lower ablation rate than observations) in the baseline experiments. The multi-model average of the estimated last day of the ablation period has a bias of about a week (last day of snow on average 5.1 days earlier than in observations). In experiments where we removed the canopy cover, the MAE averaged over models becomes 26% of the observed station-average ablation rate. The MAE of each individual model in the no-vegetation simulations is close to the baseline results: SSiB and Noah-MP have some improvement while VIC and Catchment produce slightly higher values.

2) The modeled ablation rates are highly correlated with accumulated maximum SWE in part because high SWE stations have their ablation periods at a time of year (generally later in spring than low SWE sites) when downward solar radiation, and hence net radiation, is higher. Net radiation is highly correlated with ablation rates (more so than is temperature), which is consistent with other published studies. Wind speed is not a strong predictor of ablation rates during the melting process.

3) The effects of vegetation canopy cover vary substantially across the models. The presence of a vegetation canopy increases the average ablation rates in VIC, but decreases ablation in Noah-MP, SSiB and Catchment. Under the short canopy scenario, the differences among models are mainly attributable to differences in net-radiation (Rn) estimates and energy fluxes (SH/LH) allocation. Rn is primarily affected by net shortwave radiation, which mainly results from differences in ground surface albedo in VIC, Noah-MP and Catchment. SSiB alone has large shading of incoming solar energy even for short canopies scenario, which distinguishes it from the other models.

4) If the vegetation type is switched from shrub/grass to trees, the ablation rate would become slower in VIC and faster in Noah-MP. By comparing the energy flux terms below and above trees, we also find the representation of energy allocation can be of great difference among the models. The differences in model parameterizations point to the need for observations of radiative data below and above the canopy. Given the magnitudes of the difference among models, differences in the effects of vegetation on snow ablation should be a topic for further development in the modeling community.

462 Acknowledgement: The work on which this paper was funded by NOAA Grant No.
463 NA16OAR4310139 to the University of California, Los Angeles.

464

465

466

467

468 **References**:

469 Andreadis, K. M., P. Storck, and D. P. Lettenmaier, 2009: Modeling snow accumulation and
470 ablation processes in forested environments. *Water Resour. Res.*, **45**, 1–13,
471 doi:10.1029/2008WR007042.
472 Bohn, T. J., B. Livneh, J. W. Oyler, S. W. Running, B. Nijssen, and D. P. Lettenmaier, 2013: Global
473 evaluation of MTCLIM and related algorithms for forcing of ecological and hydrological
474 models. *Agric. For. Meteorol.*, **176**, 38–49, doi:10.1016/j.agrformet.2013.03.003.
475 http://dx.doi.org/10.1016/j.agrformet.2013.03.003.
476 Chen, F., and J. Dudhia, 2001: Coupling an Advanced Land Surface–Hydrology Model with the
477 Penn State–NCAR MM5 Modeling System. Part I: Model Implementation and Sensitivity.
478 *Mon. Weather Rev.*, **129**, 569–585, doi:10.1175/1520-
479 0493(2001)129<0569:CAALSH>2.0.CO;2.
480 http://journals.ametsoc.org/doi/abs/10.1175/1520-
481 0493%282001%29129%3C0587%3ACAALSH%3E2.0.CO%3B2.
482 ——, and Coauthors, 2014: Modeling seasonal snowpack evolution in the complex terrain and
483 forested colorado headwaters region: A model intercomparison study. *J. Geophys. Res.*,
484 **119**, 13795–13819, doi:10.1002/2014JD022167.
485 Clark, M. P., and Coauthors, 2011: Representing spatial variability of snow water equivalent in
486 hydrologic and land-surface models: A review. *Water Resour. Res.*, **47**,
487 doi:10.1029/2011WR010745.
488 Cortés, G., M. Girotto, and S. Margulis, 2016: Snow process estimation over the extratropical
489 Andes using a data assimilation framework integrating MERRA data and Landsat imagery.

Water Resour. Res., **52**, 2582–2600, doi:10.1002/2015WR018376. http://doi.wiley.com/10.1002/2015WR018376.

Dozier, J., E. H. Bair, and R. E. Davis, 2016: Estimating the spatial distribution of snow water equivalent in the world's mountains. *Wiley Interdiscip. Rev. Water*, **3**, 461–474, doi:10.1002/wat2.1140. http://doi.wiley.com/10.1002/wat2.1140.

Dyer, J. L., and T. L. Mote, 2007: Trends in snow ablation over North America. *Int. J. Climatol.*, **27**, 739–748, doi:10.1002/joc.1426. http://cdiac.esd.ornl.gov/oceans/GLODAP/glodap_pdfs/Thermohaline.web.pdf.

Ek, M. B., K. E. Mitchell, Y. Lin, E. Rogers, P. Grunmann, V. Koren, G. Gayno, and J. D. Tarpley, 2003: Implementation of Noah land surface model advances in the National Centers for Environmental Prediction operational mesoscale Eta model. *J. Geophys. Res.*, **108**, 8851, doi:10.1029/2002JD003296. http://doi.wiley.com/10.1029/2002JD003296.

Guan, B., D. E. Waliser, F. M. Ralph, E. J. Fetzer, and P. J. Neiman, 2016: Hydrometeorological characteristics of rain-on-snow events associated with atmospheric rivers. *Geophys. Res. Lett.*, **43**, 2964–2973, doi:10.1002/2016GL067978.

Hamlet, A. F., and D. P. Lettenmaier, 2005: Production of Temporally Consistent Gridded Precipitation and Temperature Fields for the Continental United States. *J. Hydrometeorol.*, **6**, 330–336, doi:10.1175/JHM420.1.

Hungerford, R. D., R. R. Nemani, S. W. Running, and J. C. Coughlan, 1989: MTCLIM: a mountain microclimate simulation model. doi:10.2737/INT-RP-414. https://www.fs.usda.gov/treesearch/pubs/39815.

Kalnay, E., and Coauthors, 1996: The NCEP/NCAR 40-Year Reanalysis Project. *Bull. Am.*

Meteorol. Soc., **77**, 437–471, doi:10.1175/1520-0477(1996)077<0437:TNYRP>2.0.CO;2. http://journals.ametsoc.org/doi/abs/10.1175/1520-0477%281996%29077%3C0437%3ATNYRP%3E2.0.CO%3B2.

Li, D., M. L. Wrzesien, M. Durand, J. Adam, and D. P. Lettenmaier, 2017: How much runoff originates as snow in the western United States, and how will that change in the future? *Geophys. Res. Lett.*, **44**, 6163–6172, doi:10.1002/2017GL073551. http://doi.wiley.com/10.1002/2017GL073551.

Livneh, B., E. A. Rosenberg, C. Lin, B. Nijssen, V. Mishra, K. M. Andreadis, E. P. Maurer, and D. P. Lettenmaier, 2013: A long-term hydrologically based dataset of land surface fluxes and states for the conterminous United States: Update and extensions. *J. Clim.*, **26**, 9384–9392, doi:10.1175/JCLI-D-12-00508.1. http://journals.ametsoc.org/doi/abs/10.1175/JCLI-D-12-00508.1 (Accessed October 22, 2014).

Lundquist, J. D., S. E. Dickerson-Lange, J. A. Lutz, and N. C. Cristea, 2013: Lower forest density enhances snow retention in regions with warmer winters: A global framework developed from plot-scale observations and modeling. *Water Resour. Res.*, **49**, 6356–6370, doi:10.1002/wrcr.20504.

Magand, C., A. Ducharne, N. Le Moine, and S. Gascoin, 2013: Introducing Hysteresis in Snow Depletion Curves to Improve the Water Budget of a Land Surface Model in an Alpine Catchment. *J. Hydrometeorol.*, **15**, 631–649, doi:10.1175/jhm-d-13-091.1.

Moore, R. D., and I. F. Owens, 1984: Controls on Advective Snowmelt in a Maritime Alpine Basin. *J. Clim. Appl. Meteorol.*, **23**, 135–142, doi:10.1175/1520-0450(1984)023<0135:coasia>2.0.co;2.

534 Mote, P. W., A. F. Hamlet, M. P. Clark, and D. P. Lettenmaier, 2005: Declining Mountain
535 Snowpack in Western North America*. *Bull. Am. Meteorol. Soc.*, **86**, 39–49,
536 doi:10.1175/BAMS-86-1-39.
537 ——, S. Li, D. P. Lettenmaier, M. Xiao, and R. Engel, 2018: Dramatic declines in snowpack in the
538 western US. *npj Clim. Atmos. Sci.*, **1**, 2, doi:10.1038/s41612-018-0012-1.
539 http://www.nature.com/articles/s41612-018-0012-1.
540 Musselman, K. N., M. P. Clark, C. Liu, K. Ikeda, and R. Rasmussen, 2017: Slower snowmelt in a
541 warmer world. *Nat. Clim. Chang.*, doi:10.1038/nclimate3225.
542 Newman, A. J., M. P. Clark, A. Winstral, D. Marks, and M. Seyfried, 2014: The Use of Similarity
543 Concepts to Represent Subgrid Variability in Land Surface Models: Case Study in a
544 Snowmelt-Dominated Watershed. *J. Hydrometeorol.*, **15**, 1717–1738, doi:10.1175/JHM-D-
545 13-038.1. http://journals.ametsoc.org/doi/abs/10.1175/JHM-D-13-038.1.
546 Niu, G.-Y., and Z.-L. Yang, 2007: An observation-based formulation of snow cover fraction and
547 its evaluation over large North American river basins. *J. Geophys. Res.*, **112**, D21101,
548 doi:10.1029/2007JD008674. http://doi.wiley.com/10.1029/2007JD008674.
549 Niu, G. Y., and Coauthors, 2011: The community Noah land surface model with
550 multiparameterization options (Noah-MP): 1. Model description and evaluation with local-
551 scale measurements. *J. Geophys. Res. Atmos.*, **116**, 1–19, doi:10.1029/2010JD015139.
552 Oaida, C. M., Y. Xue, M. G. Flanner, S. M. Skiles, F. De Sales, and T. H. Painter, 2015: Improving
553 snow albedo processes in WRF/SSiB regional climate model to assess impact of dust and
554 black carbon in snow on surface energy balance and hydrology over western U.S. *J.*
555 *Geophys. Res. Atmos.*, **120**, 3228–3248, doi:10.1002/2014JD022444.

http://doi.wiley.com/10.1002/2014JD021636.

Oyler, J. W., S. Z. Dobrowski, A. P. Ballantyne, A. E. Klene, and S. W. Running, 2015: Artificial amplification of warming trends across the mountains of the western United States. *Geophys. Res. Lett.*, **42**, 153–161, doi:10.1002/2014GL062803. http://widgets.ebscohost.com/prod/customlink/hanapi/hanapi.php?profile=4dfs1q6ik%2BHE5pTp1ZLu0eGT1tTR28jqzaLXyajL2dTV482lyNzZoJmu5NS8q%2BnpkKU%3D&DestinationURL=http%3A%2F%2Fsearch.ebscohost.com%2Flogin.aspx%3Fdirect%3Dtrue%26db%3Dpsyh%26AN%3D2011-17722-0.

Painter, T. H., S. M. K. Skiles, J. S. Deems, W. T. Brandt, and J. Dozier, 2018: Variation in Rising Limb of Colorado River Snowmelt Runoff Hydrograph Controlled by Dust Radiative Forcing in Snow. *Geophys. Res. Lett.*, **45**, 797–808, doi:10.1002/2017GL075826.

Rauscher, S. A., J. S. Pal, N. S. Diffenbaugh, and M. M. Benedetti, 2008: Future changes in snowmelt-driven runoff timing over the western US. *Geophys. Res. Lett.*, **35**, 1–5, doi:10.1029/2008GL034424.

Rutter, N., and Coauthors, 2009: Evaluation of forest snow processes models (SnowMIP2). *J. Geophys. Res.*, **114**, D06111, doi:10.1029/2008JD011063. http://doi.wiley.com/10.1029/2008JD011063.

Sellers, P. J., C. J. Tucker, G. J. Collatz, S. O. Los, C. O. Justice, D. A. Dazlich, and D. A. Randall, 1996: A Revised Land Surface Parameterization (SiB2) for Atmospheric GCMS. Part II: The Generation of Global Fields of Terrestrial Biophysical Parameters from Satellite Data. *J. Clim.*, **9**, 706–737, doi:10.1175/1520-0442(1996)009<0706:ARLSPF>2.0.CO;2. http://journals.ametsoc.org/doi/abs/10.1175/1520-

578 0442%281996%29009%3C0706%3AARLSPF%3E2.0.CO%3B2.
579 Shi, X., S. J. Déry, P. Y. Groisman, and D. P. Lettenmaier, 2013: Relationships between recent
580 pan-arctic snow cover and hydroclimate trends. *J. Clim.*, **26**, 2048–2064, doi:10.1175/JCLI-
581 D-12-00044.1. http://journals.ametsoc.org/doi/abs/10.1175/JCLI-D-12-00044.1.
582 Stieglitz, M., A. Ducharne, R. Koster, and M. Suarez, 2001: The Impact of Detailed Snow Physics
583 on the Simulation of Snow Cover and Subsurface Thermodynamics at Continental Scales. *J.*
584 *Hydrometeorol.*, **2**, 228–242, doi:10.1175/1525-7541(2001)002<0228:TIODSP>2.0.CO;2.
585 Sturm, M., J. Holmgren, and G. E. Liston, 1995: A Seasonal Snow Cover Classification System for
586 Local to Global Applications. *J. Clim.*, **8**, 1261–1283, doi:10.1175/1520-
587 0442(1995)008<1261:ASSCCS>2.0.CO;2.
588 http://journals.ametsoc.org/doi/abs/10.1175/1520-
589 0442%281995%29008%3C1261%3AASSCCS%3E2.0.CO%3B2.
590 Sun, S., J. Jin, and Y. Xue, 1999: A simple snow-atmosphere-soil transfer model. *J. Geophys. Res.*,
591 **104**, 587–597.
592 Tan, A., J. C. Adam, and D. P. Lettenmaier, 2011: Change in spring snowmelt timing in Eurasian
593 Arctic rivers. *J. Geophys. Res.*, **116**, D03101, doi:10.1029/2010JD014337.
594 Trujillo, E., and N. P. Molotch, 2014: Snowpack regimes of the Western United States. *Water*
595 *Resour. Res.*, **50**, 5611–5623, doi:10.1002/2013WR014753.
596 http://doi.wiley.com/10.1002/2013WR014753.
597 USACE, 1956: *Snow hydrology summary report of the snow investigations. North Pacific Division*
598 *Portland*.
599 Verseghy, D. L., 1991: Class-A Canadian land surface scheme for GCMS. I. Soil model. *Int. J.*

Climatol., **11**, 111–133, doi:10.1002/joc.3370110202.
http://doi.wiley.com/10.1002/joc.3370110202.

Waliser, D., and Coauthors, 2011: Simulating cold season snowpack: Impacts of snow albedo and multi-layer snow physics. *Clim. Change*, **109**, 95–117, doi:10.1007/s10584-011-0312-5.

Xia, Y., D. Mocko, M. Huang, X. Cai, M. Rodell, K. E. Mitchell, M. B. Ek, and B. Li, 2016: Comparison and Assessment of Three Advanced Land Surface Models in Simulating Terrestrial Water Storage Components over the United States. *J. Hydrometeorol.*, **18**, 625–649, doi:10.1175/jhm-d-16-0112.1.

Xue, Y., S. Sun, D. S. Kahan, and Y. Jiao, 2003: Impact of parameterizations in snow physics and interface processes on the simulation of snow cover and runoff at several cold region sites. *J. Geophys. Res.*, **108**, 8859, doi:10.1029/2002JD003174.
http://doi.wiley.com/10.1029/2002JD003174.

Xue, Y., B. A. Forman, and R. H. Reichle, 2018: Estimating Snow Mass in North America Through Assimilation of Advanced Microwave Scanning Radiometer Brightness Temperature Observations Using the Catchment Land Surface Model and Support Vector Machines. *Water Resour. Res.*, **54**, 6488–6509, doi:10.1029/2017WR022219.

Table 1: Site locations and attributes for the selected SNOTEL sites.

Site #	Station name	Lon	Lat	State	Elevation (m)
1	Olallie Meadows	-121.44	47.37	WA	1228
2	Hand Creek	-114.84	48.31	MT	1535
3	Pike Creek	-113.33	48.30	MT	1808
4	Hemlock Butte	-115.63	46.48	ID	1771
5	Banner Summit	-115.23	44.30	ID	2146
6	Blue Mountain Spring	-118.52	44.25	OR	1789
7	Silver Creek	-121.18	42.96	OR	1750
8	Central Sierra Snow Laboratory	-120.37	39.33	CA	2101
9	Leavitt Meadows	-119.55	38.30	CA	2194
10	Schofield Pass	-107.05	39.02	CO	3261

627

628 Table 2: Key features of the snow-related physics in the four Land Surface Models.

	VIC	Noah-MP	SSiB	Catchment
Snow albedo decay	Yes	Yes	Yes	Yes
Canopy interception	Liquid and snow	Liquid and snow	Liquid and snow	Liquid and snow
Canopy radiation transfer	Two streams	Two streams	Two streams	Tile average
Max snow layers	2-layer	3-layer	3-layer	3-layer
Canopy attenuation of solar radiation	Yes	Yes	Yes	Yes
Canopy attenuation of wind	Yes	Yes	Yes	No

629

630 Table 3: Climatology of average April-July daily temperature (T), annual maximum SWE and
631 average temperature during ablation as defined in section 2.1 at selected stations over 1992-
632 2012.

#	Station name	Avg Apr-Jul T (˚C)	Avg SWE (mm)	Avg T during melt period (˚C)
1	Olallie Meadows	7.3	1492	7.4
2	Hand Creek	8.7	299	4.1
3	Pike Creek	8.0	628	6.6
4	Hemlock Butte	8.8	1224	8.5
5	Banner Summit	7.3	673	5.4
6	Blue Mountain Spring	8.9	434	4.0
7	Silver Creek	9.8	322	3.1
8	Central Sierra Snow Laboratory	8.8	1066	4.7
9	Leavitt Meadows	10.0	345	2.5
10	Schofield Pass	5.6	998	5.3

633
634
635
636
637

638
639

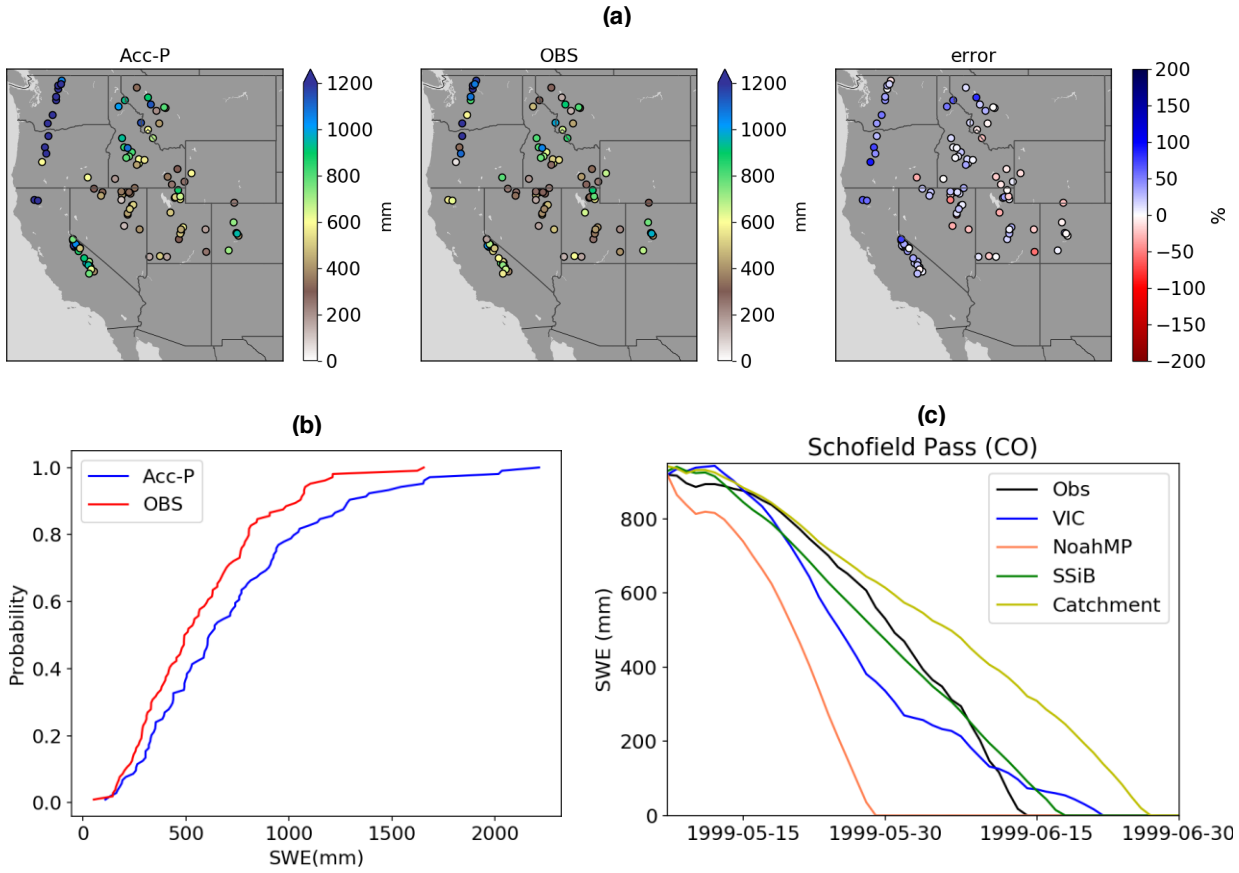

640

641 Figure 1: (a) Climatology of annual maximum SWE estimated by accumulated precipitation below
642 0˚C (Acc-P), observations (OBS) percent error for 1986-2005 averaged over ~100 SNOTEL stations.
643 (b) Empirical cumulative probability curves for annual maximum SWE from observations (OBS)
644 and accumulated precipitation (ACC-P) over all the stations in (a). (c) Observed and simulated
645 SWE time-series plot for Schofield Pass, CO for spring 1999. The models are all initialized with the
646 observed maximum SWE on May 07th, 1999.

647

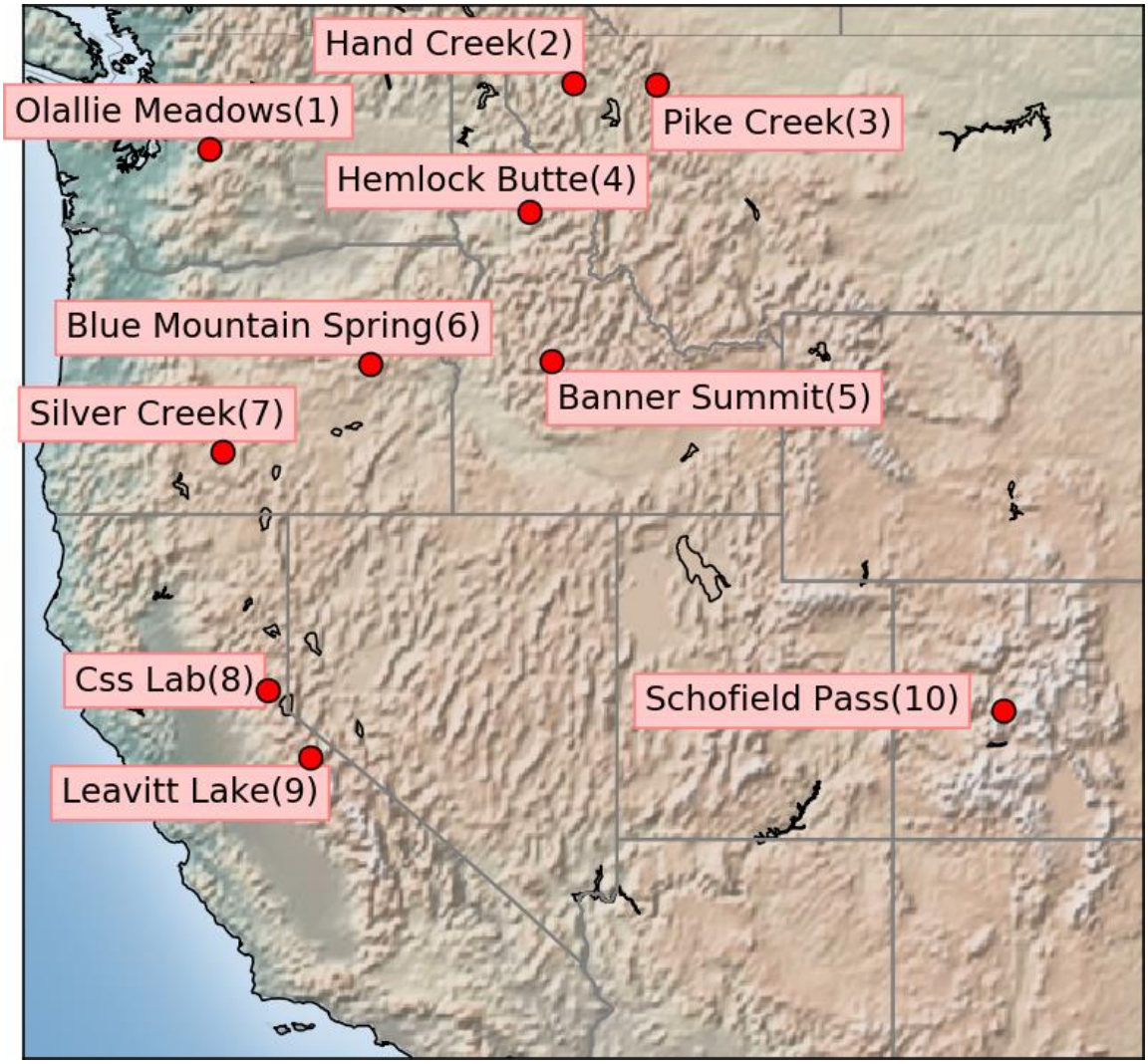

Figure 2: Selected NRCS SNOTEL stations over the Western U.S. The names and index numbers correspond to the information given in Table 1.

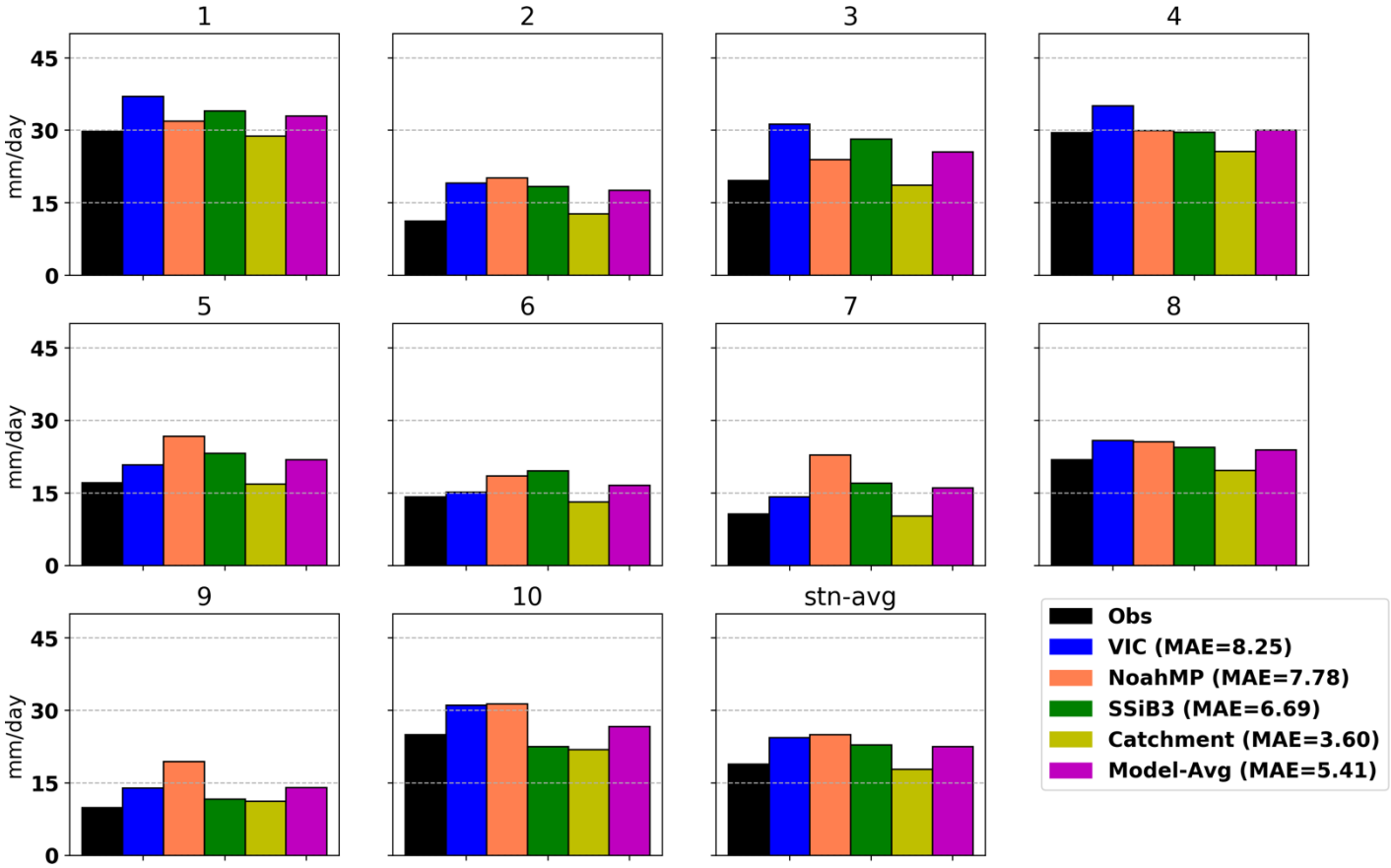

652

653 Figure 3: Snow ablation rates at the 10 SNOTEL sites averaged over 1992s-2012. Index numbers

654 correspond to Table 1; “stn-avg” is the mean over all stations.

655

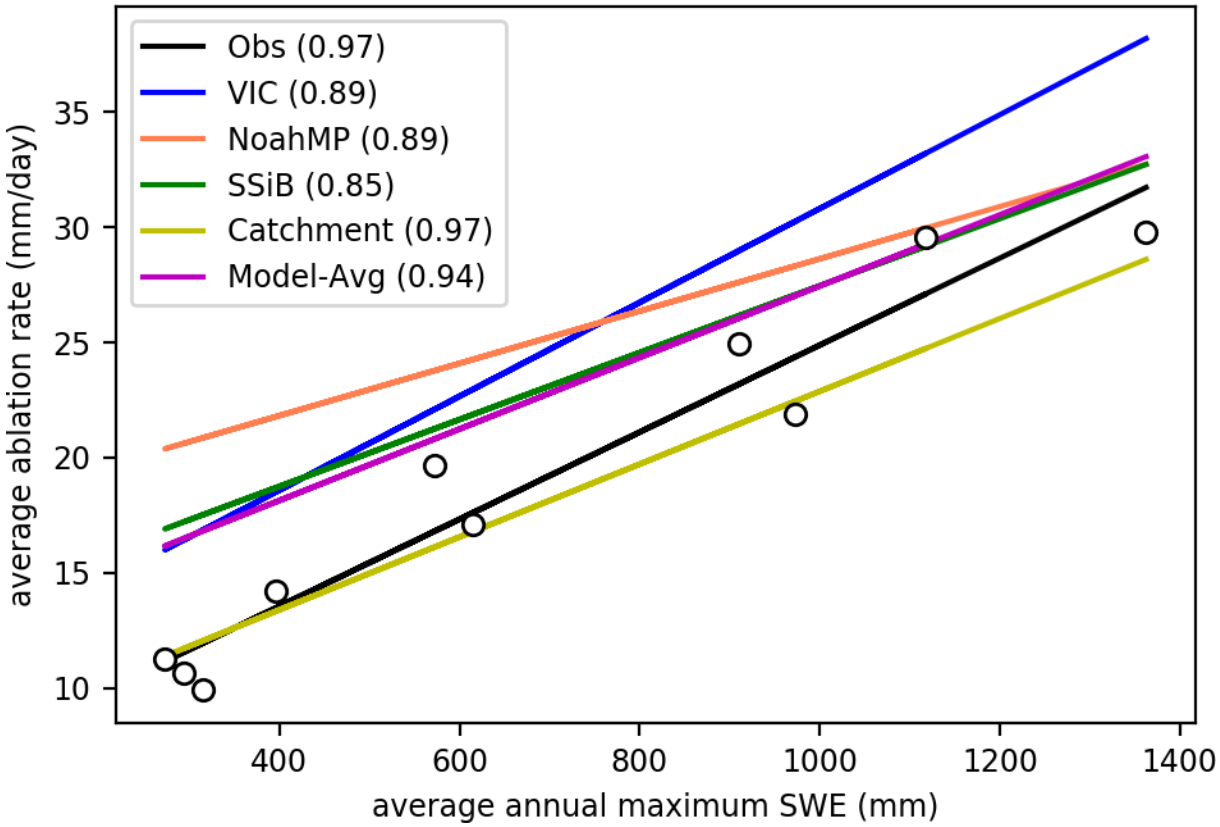

656
657

658 Figure 4: Linear regressions between annual maximum SWE (climatological mean) and average

659 melt rates over the 10 sites. The legend provides the correlation coefficients. The circles are the

660 mean observed melt rate vs mean observed SWE.

661

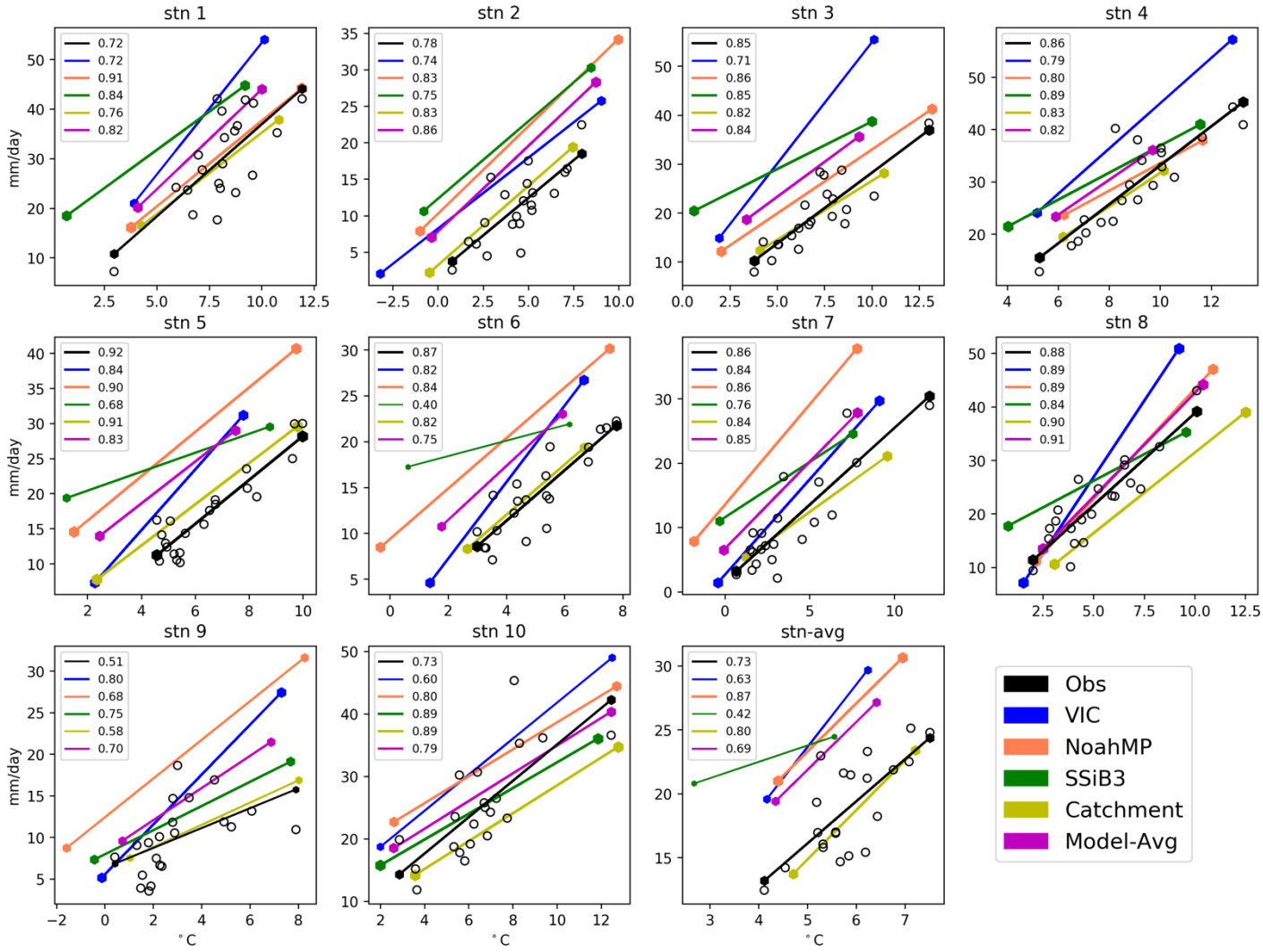

Figure 5: Linear regressions of melt rate vs. average temperature during the melt period across all stations for both observations and simulations (correlation coefficients are given in the legend). The black circles are the observed ablation rates. The ablation units are mm/day (temperature in ˚C). Larger plot symbols indicate higher r-values.

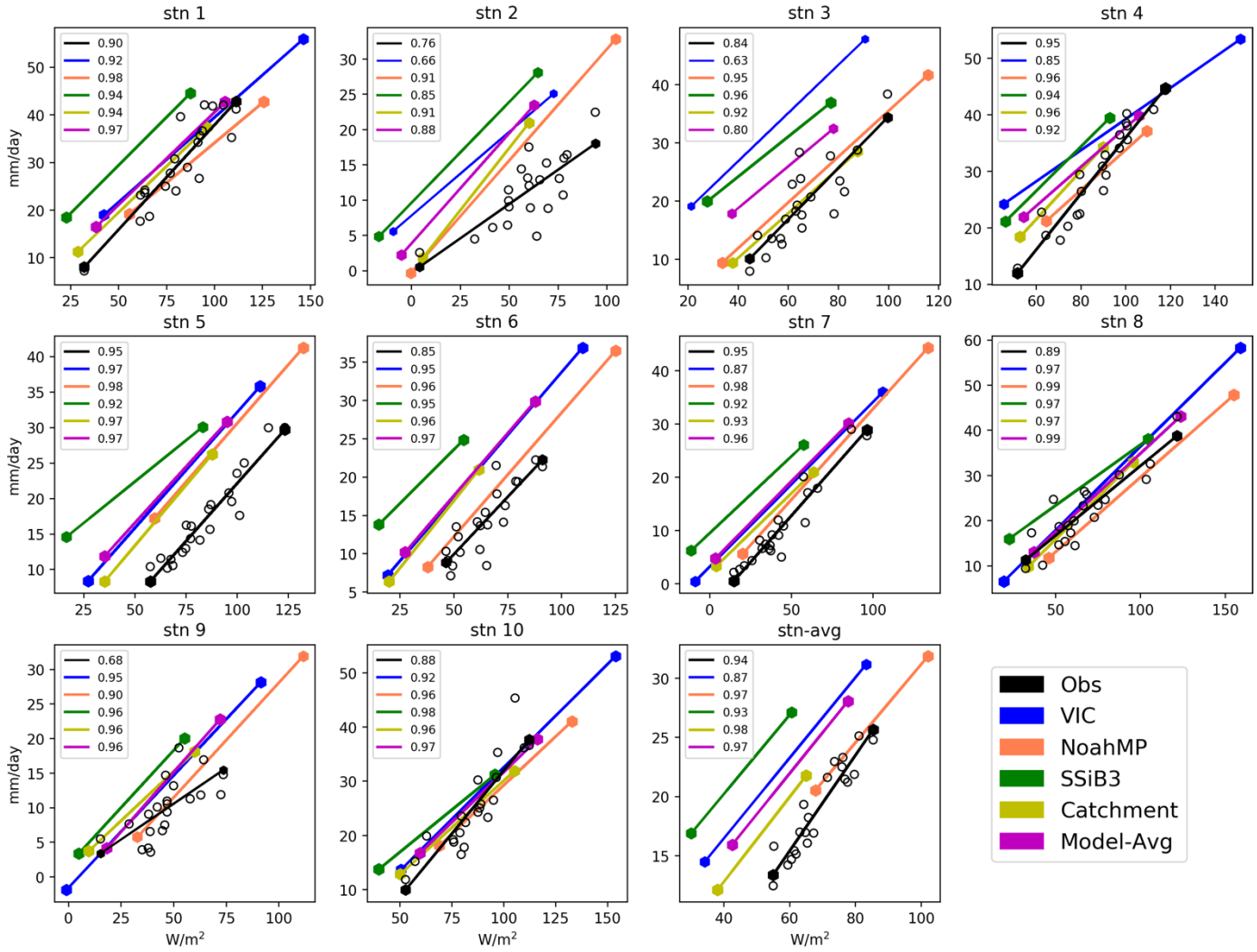

669

670 Figure 6: Same as Figure 5 but for temperature replaced by net radiation. For the 'Obs' curves we

671 used model-averaged net radiation as a surrogate for observations. Net radiation units are

672 W/m^2.

673

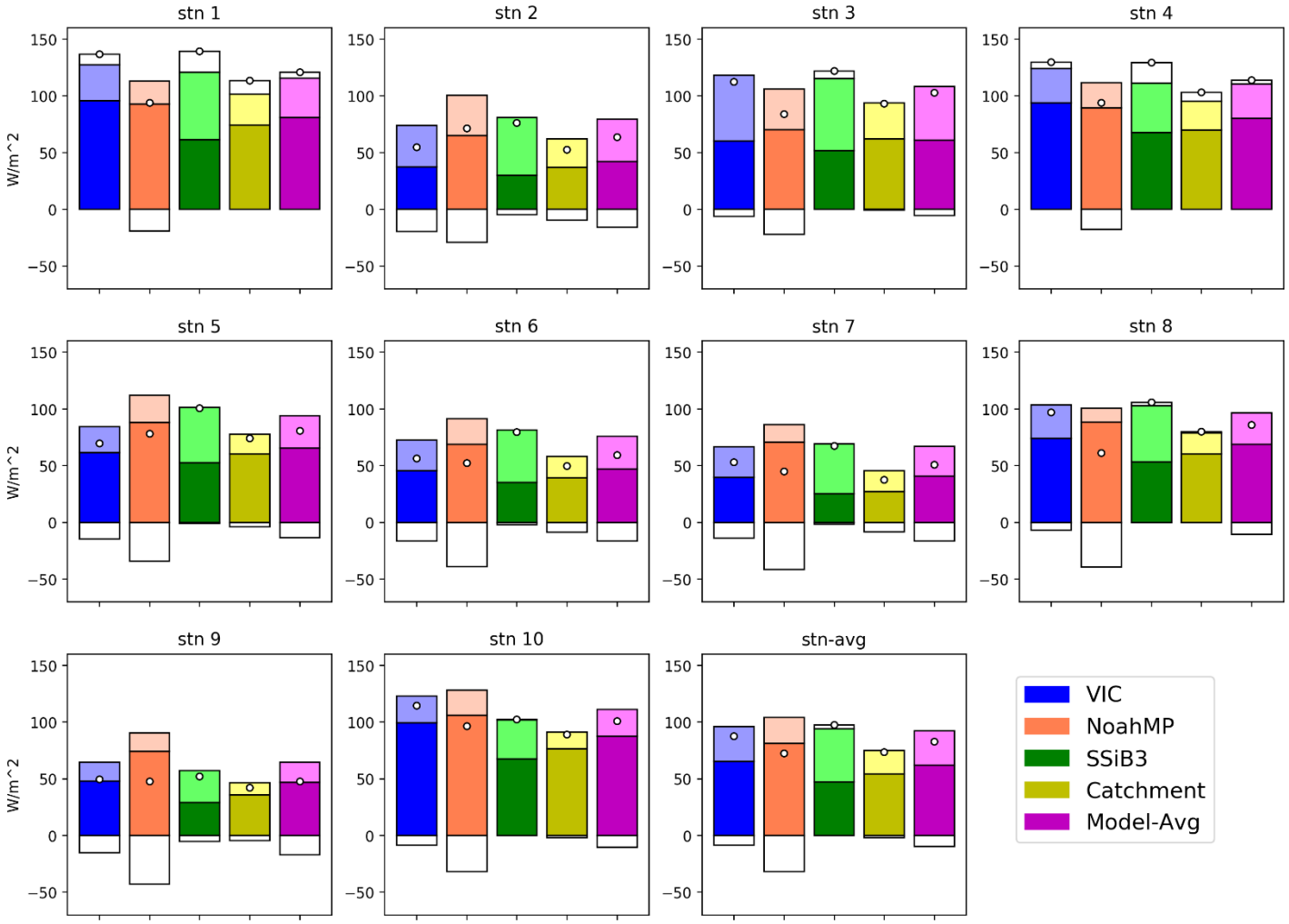

Figure 7: Energy components at snow surface for each of the 10 SNOTEL stations. The deep colored bars indicate net radiation (Rn), the white bars are the latent heat (LH), and the shaded bars are the sensible heat (SH). The white dots indicate the energy difference term, Q_M (Rn+LH+SH). All units are W/m^2.

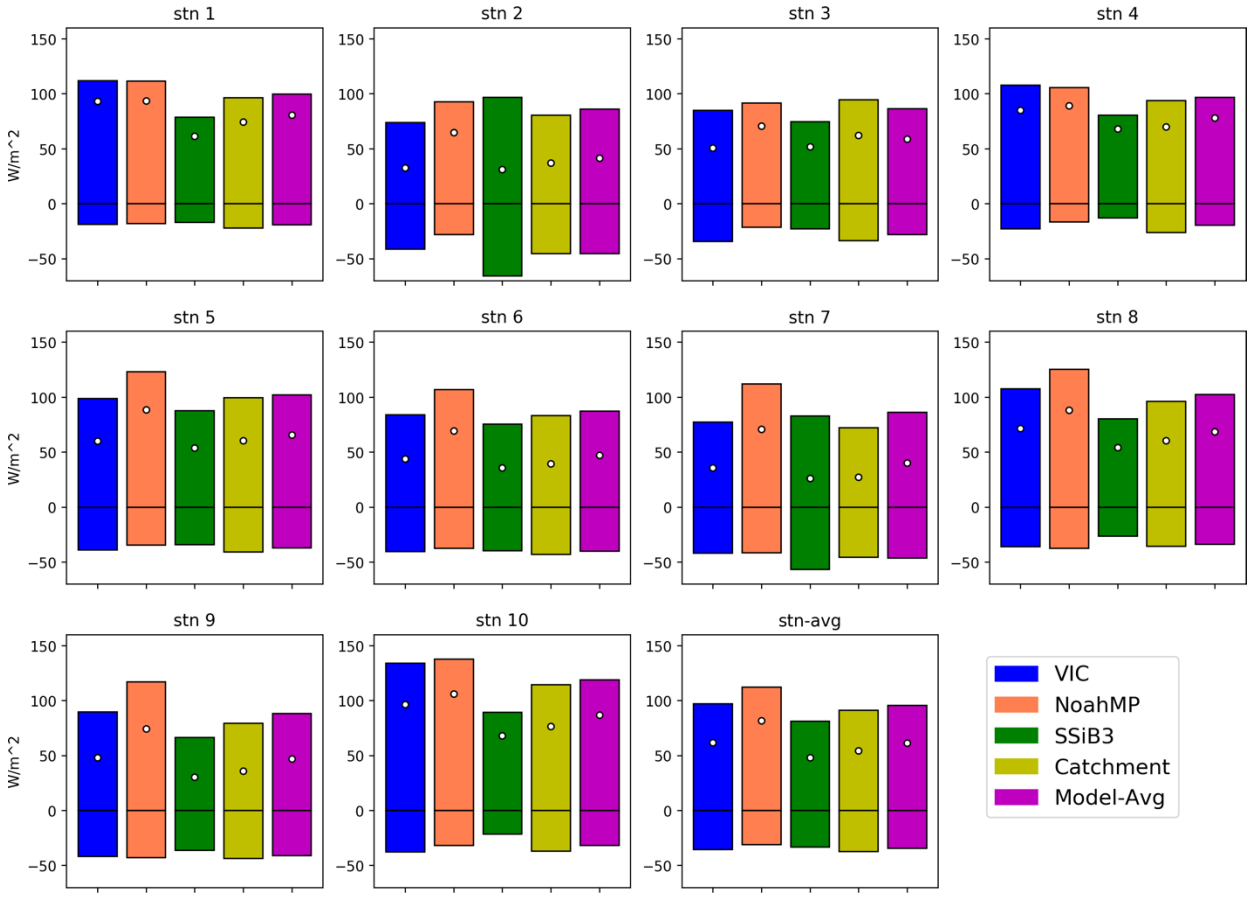

Figure 8: Snow surface downward net shortwave (positive) and net longwave (negative) radiation in W/m^2 over all the SNOTEL sites. White circles indicate the net radiation (i.e. net shortwave minus net longwave) term.

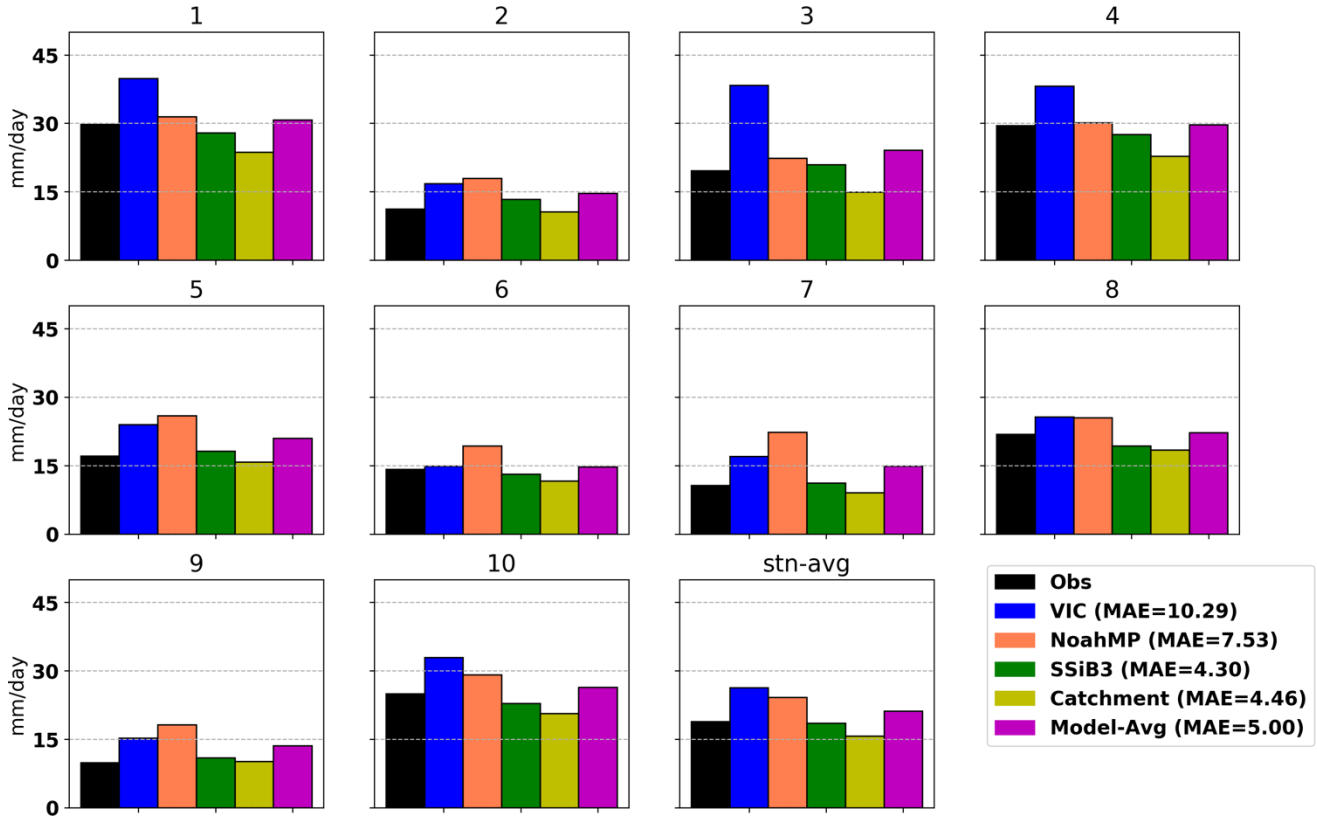

686

687 Figure 9: Same as Figure 3 but results are extracted from no vegetation experiment.

688

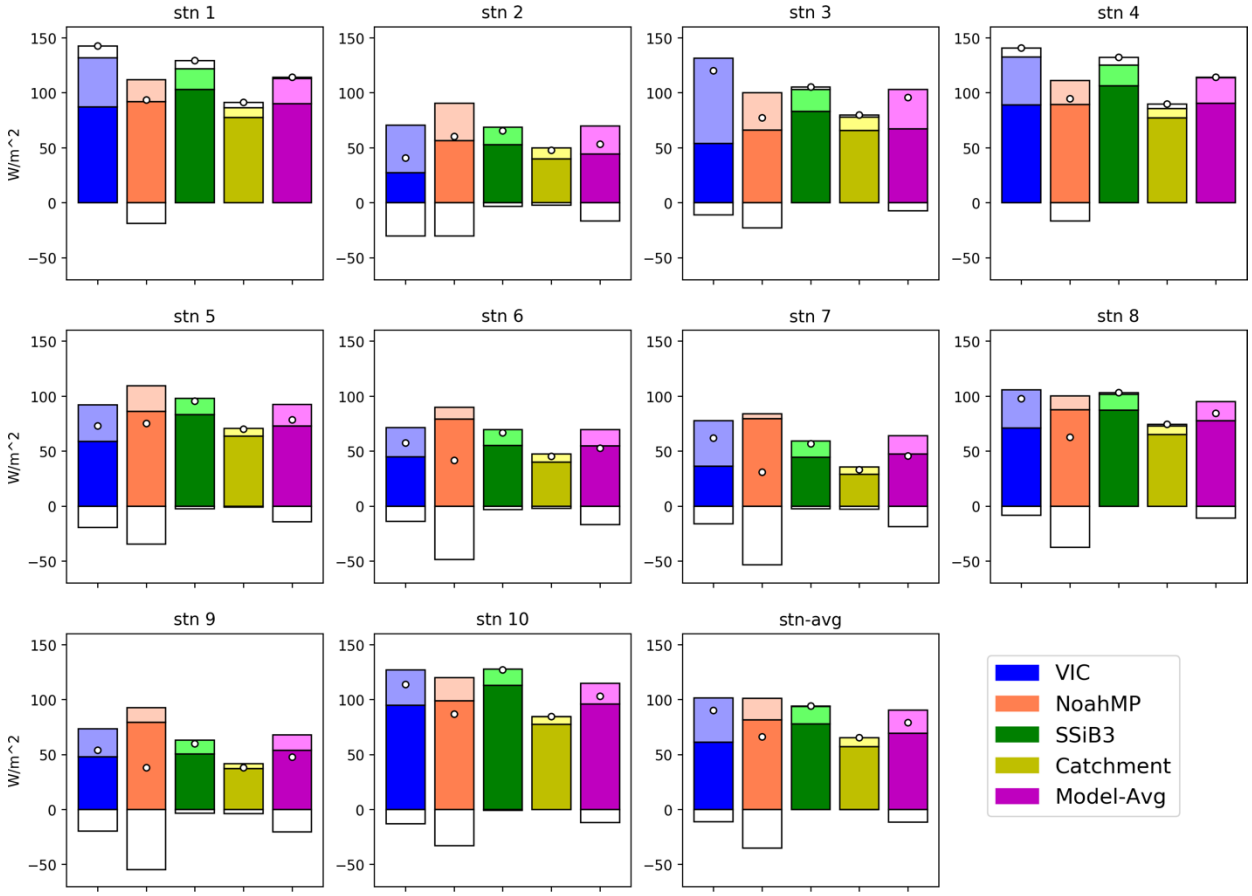

689

690 Figure 10: Same as Figure 7 but results are extracted from no vegetation experiment.

691

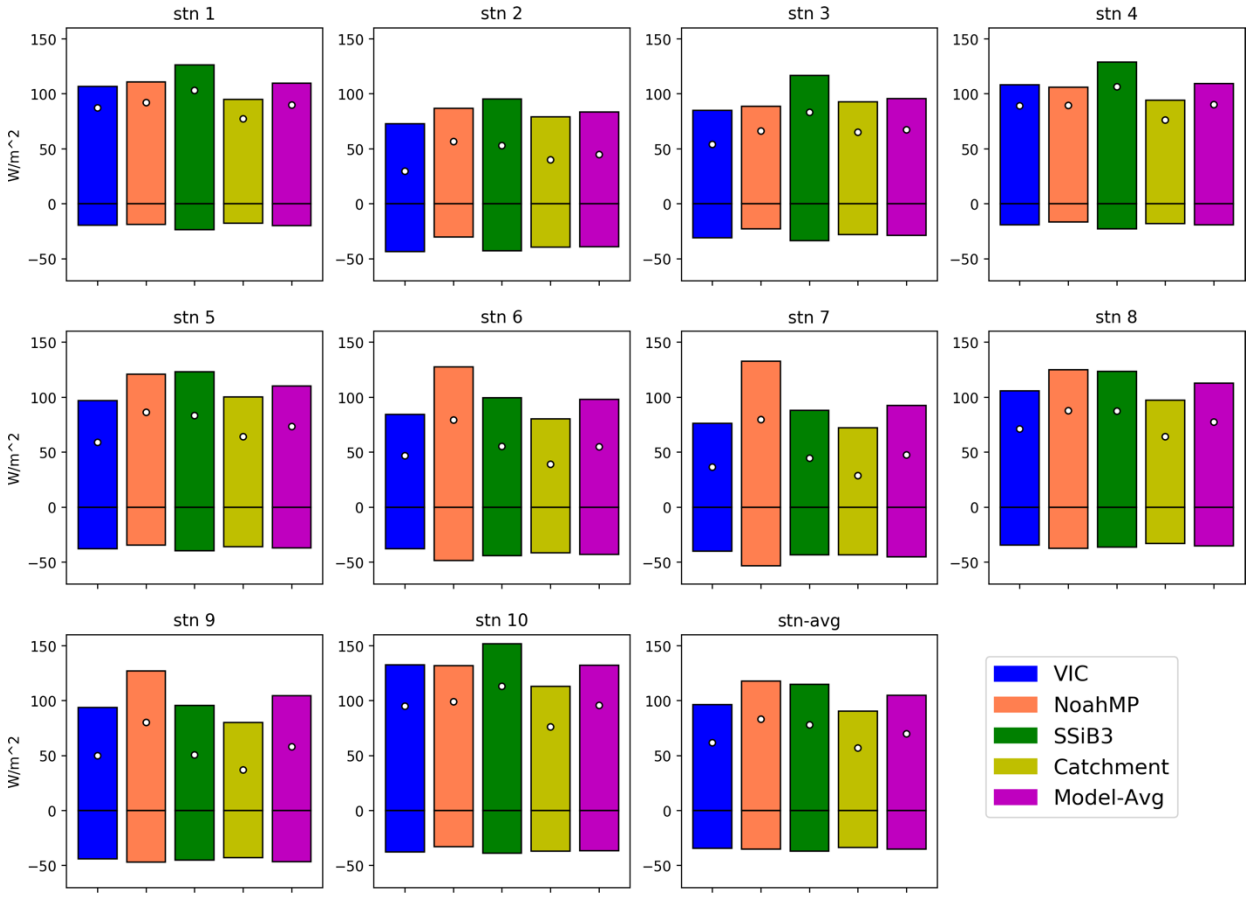

692

693 Figure 11: Same as Figure 8 but the results are extracted from no vegetation experiment.

694

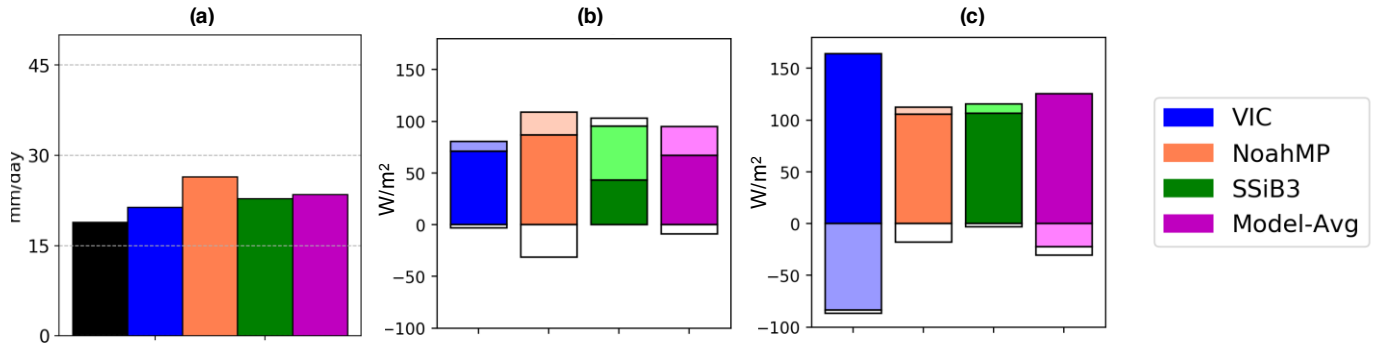

Figure 12: (a) Station-average ablation rate extracted from tree-scenario simulation. The black bar is calculated from observation, same as in Figure 3. (b) Energy flux terms for tree experiment (as in Fig.7) for VIC, Noah-MP and SSiB3 for snow surface. (c) same as (b) but for fluxes at top of the canopy. Results for Catchment not shown for reasons indicated in Section 4.2.